Proceedings of the ASME 2024
International Mechanical Engineering Congress and Exposition
IMECE2024
November 17-21, 2024, Portland, Oregon

IMECE2024-146008

MANUFACTURING, CHARACTERIZATION AND TERRESTRIAL PASSIVE RADIATIVE COOLING PERFORMANCE OF NANOFIBROUS PTFE-PEO COMPOSITE THERMAL COATINGS

Chieloka Ibekwe[1], Xuanjie Wang[1], Jason W. Hartwig[2], Adam M. Swanger[3], and Shankar Narayan[1]

[1]Rensselaer Polytechnic Institute, Troy, NY, 12180, USA
[2]NASA Glenn Research Center, Cleveland, OH, 44135, USA
[3] NASA Kennedy Space Center, FL, 32899, USA

ABSTRACT

Passive heat management is desirable in many applications since it can reduce the energy expended for cooling, for example, in buildings and automobiles. Specifically, materials with wavelength-dependent reflectance and emittance can manage incident solar fluxes while enabling passive radiative cooling by thermal emission. This study demonstrates the use of polymeric nanofibers, specifically polytetrafluoroethylene (PTFE) and polyethylene oxide (PEO) composite, as thermal coatings for passive temperature control. Employing the electrospinning fabrication process, we engineer nano and micro-scale fibrous structures, studying the influence of fabrication parameters, such as precursor material concentration and rotating collector speed, on fiber geometry and optical properties. To understand the role of material and fiber geometry on optical performance, we characterize various samples' spectral reflectance, absorptance, and transmittance using spectrophotometers interfaced with integrating spheres. The results show the potential of nanofabricated PTFE-PEO coatings as promising candidates for passive thermal control. We highlight their competitive edge by comparing their solar reflectance and emittance values to existing passive radiative thermal control materials. In essence, this study contributes to advancing passive heat management technologies, offering insights into optimizing material composition and fabrication techniques for enhanced performance in various applications.

Keywords: micro and nano-engineered materials, spectrally selective materials, passive radiative cooling, solar reflectance, thermal emittance, passive thermal control, building heat

1. INTRODUCTION

Passive thermal control offers a method to regulate system temperature without requiring significant energy input [1]. Traditional temperature regulation methods in buildings, such as air conditioners, entail high energy consumption and cost [2]. Additionally, these systems often utilize refrigerants that emit environmentally harmful volatile compounds. Incorporating passive systems presents an opportunity to reduce reliance on active thermal control methods and achieve energy and cost savings.

Considerable research has been devoted to exploring passive thermal control methods for passive radiative cooling. Zhou et al. (2021) utilized porous polyethylene embedded with silica particles, achieving a cooling power of 85 W/m^2 [3]. Similarly, Chen et al. (2021) engineered a mesoporous photonic structure using polyvinylidenefluoride-co-hexafluoropropylene, yielding a cooling performance of 72 W/m^2 [4]. Wang et al. (2022) combined polytetrafluoroethylene and a spectrally selective absorber to form a multilayered structure with thermal radiative switching abilities for solar-thermal regulation, capable of switching between reflecting and absorbing modes, allowing a 51 ℃ temperature change [5]. Other materials of interest include polyester fabrics [6], glass bubbles in a polydimethylsiloxane matrix [7], barium sulphate dispersed in polyvinylidenefluoropropylene [8], silicon dioxide spheres in a polymethylpentene matrix [9], polyethylene oxide [10], and hierarchically layered hafnium (IV) oxide and silicon dioxide [11].

Many techniques have been shown to yield materials with specific nanostructures and surface morphologies [5,12–17] for high solar reflectance (or low solar absorptance) in the solar spectrum (0.3-2.5 μm) and high thermal emittance in the long-wave infrared (LWIR) atmospheric transmission window (8-13 μm). This atmospheric window permits the outward emission of

thermal radiation from Earth to outer space at temperatures close to 3 K [4,18–24]. By combining these desirable optical characteristics, self-cooling can be achieved without the need for substantial active energy consumption.

This study introduces a method for passive thermal control utilizing nano and micro-scale fibrous and porous coating materials with exceptionally high solar reflectance (incredibly low solar absorptance) and large thermal emittance in LWIR. These materials are fabricated using electrospinning - a well-established nanofabrication technique [16,25–34]. We investigate how variations in process parameters, such as precursor material concentration and rotating collector speed, impact fiber geometry and optical properties. Through a comparative analysis of average solar reflectance and thermal emittance values with state-of-the-art materials, our nanofabricated PTFE-PEO coatings demonstrate significant potential as passive radiative thermal control material.

2. MATERIALS AND METHODS

2.1 Materials and Solution

The composite PTFE-PEO solution was prepared by dissolving PEO powder in deionized water, stirring at 60 ℃ and 600 rpm until the powder was fully dissolved and a viscous clear solution of PEO was formed. To this solution, we added PTFE dispersion and allowed the solution to properly mix for 4 to 6 hours, at room temperature. Subsequently, the composite solution was loaded into a syringe for use in the electrospinning process.

2.2 Fabrication

The electrospinning setup comprises a high-voltage power source, a grounded rotating collector, a syringe pump, a syringe containing the composite solution, a needle, and a DC motor for rotary motion, as depicted in Figure 1.

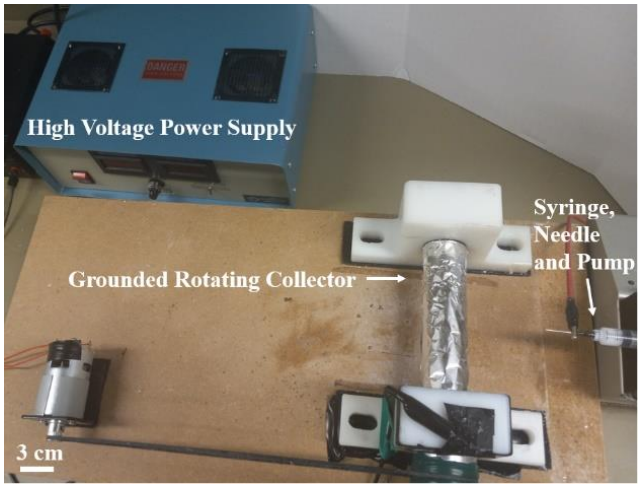

Figure 1: Electrospinning setup.

Under standard conditions (baseline), the following fabrication parameters were used: a potential of 10 kV between the needle and the earthed collector, a flow rate of 8.33 µl/min, a distance of 12 cm between the collector and the needle, and a collector speed of 500 rpm. Initially, the pump and DC motor were activated, followed by the high-voltage source. As the voltage was gradually increased to its maximum, the solution at the needle's tip underwent deformation, transitioning from its initial hemispherical shape to a conical form (known as the Taylor cone). Subsequently, polymeric fibers were extruded from the tip of the needle and collected onto the rotating collector.

2.3 Characterization

Scanning Electron Microscopy (SEM) images were captured using a Carl Zeiss Supra 55 Field Emission Scanning Electron Microscope (FESEM) with a working distance of 3 mm and an accelerating voltage of 1.5 kV. The obtained SEM images were processed and analyzed using Image J software.

The spectral normal-hemispherical reflectance and transmittance of the samples in the 300-2500 nm wavelength range were characterized using a Perkin-Elmer Lambda 950 UV-Visible-NIR spectrometer equipped with a 6-inch Spectralon® integrating sphere. For the reflectance measurements, each sample was placed normal to the reflectance port and the light beam irradiated the sample at an 8˚ angle of incidence. The average solar reflectance was calculated using the following equation,

$$\rho_{solar} = \frac{\int_{\lambda=0.3\ \mu m}^{\lambda=2.5\ \mu m} \rho(\lambda)\ I_{solar}(\lambda) d\lambda}{\int_{\lambda=0.3\ \mu m}^{\lambda=2.5\ \mu m} I_{solar}(\lambda) d\lambda} \quad (1)$$

where $\rho(\lambda)$ represents the spectral normal-hemispherical reflectance obtained from the spectrometer relative to Spectralon's® spectral reflectance, and $I_{solar}(\lambda)$ is the solar spectral intensity using the ASTM G173 Air Mass 1.5 terrestrial solar spectrum.

The spectral optical properties in the long-wave infrared (LWIR) atmospheric transmission window (8-13 µm) were characterized using a Fourier-Transform Infrared spectrometer (ThermoFisher Scientific Nicolet™ iS20) equipped with a 3-inch gold-coated integrating sphere (Pike Technologies Mid-IR IntegratIR™) and a mercury cadmium telluride (MCT) detector. The average emittance of the materials was calculated using the following equation,

$$\varepsilon_{LWIR} = \frac{\int_{\lambda=8\ \mu m}^{\lambda=13\ \mu m} \left(\varepsilon_{LWIR}(\lambda)\right) E_{b\lambda}(\lambda,T)\, d\lambda}{\int_{\lambda=8\ \mu m}^{\lambda=13\ \mu m} E_{b\lambda}(\lambda,T)\, d\lambda} \quad (2)$$

where $\varepsilon_{LWIR} = 1 - \rho_{LWIR}(\lambda)$ represents the spectral normal-hemispherical emittance and $E_{b\lambda}(\lambda,T)$ is the spectral blackbody emissive radiance, as shown:

$$E_{b\lambda}(\lambda,T) = \frac{2hc^2}{\lambda^5\left(e^{\frac{hc}{\lambda K_B T}} - 1\right)} \quad (3)$$

Here h, c, λ, K_B, T represent Planck's constant, speed of light in vacuum, wavelength, Boltzmann's constant, and absolute temperature of the blackbody, respectively.

2.4. Radiative Cooling Power Analysis

We conducted the following analysis to assess the cooling capacity of the radiative cooling materials assessed in this study. When exposed to the sky during daytime at a temperature T, a material of surface area A, would receive solar irradiance as well as atmospheric radiation (equivalent to the ambient temperature, T_{amb}). The material would also experience parasitic heat fluxes due to thermal conduction and atmospheric convection, and the net radiative cooling power of the material (P_{net}) is given by:

$$P_{net}(T) = P_{out}(T) - P_{atm}(T_{amb}) - P_{sol} - P_{par} \quad (4)$$

The power radiated outward $P_{out}(T)$ by the material is:

$$P_{out}(T) = A \int d\Omega cos\theta \int_0^\infty d\lambda \varepsilon(\lambda) E_{b\lambda}(\lambda, T) \quad (5)$$

where $\int d\Omega = \int_0^{2\pi} \int_0^{\pi/2} d\theta sin\theta d\varphi$ is the angular integral over a hemisphere and $E_{b\lambda}(\lambda)$ is the spectral blackbody emissive radiance at temperature T.

The atmospheric thermal radiation absorbed by the material is given by:

$$P_{atm}(T_{amb}) = A \int d\Omega cos\theta \int_0^\infty d\lambda \varepsilon(\lambda) \varepsilon_{atm}(\lambda) E_{b\lambda}(\lambda, T_{amb}) \quad (6)$$

where $\varepsilon_{atm}(\lambda)$ is directional emissivity of the atmosphere given by the following equation,

$$\varepsilon_{atm}(\lambda) = 1 - \tau_{atm}(\lambda)^{1/cos\theta} \quad (7)$$

and $\tau_{atm}(\lambda)^{1/cos\theta}$ is the atmospheric transmittance in the normal direction.

The absorbed solar power is given by:

$$P_{sol} = \mathrm{A} \int_0^\infty d\lambda \varepsilon(\lambda) I_{solar}(\lambda) \quad (8)$$

Using Kirchhoff's radiation law, and assuming a diffuse surface, $\varepsilon(\lambda) = \alpha(\lambda)$ where $\alpha(\lambda)$ is the spectral solar absorptance.

The parasitic heat flux is estimated as:

$$P_{par} = A h_c (T_{amb} - T) \quad (9)$$

where h_c is the non-radiative, combined heat transfer coefficient to account for both conduction through support structures and convection to the ambient air.

This study calculates the net cooling power P_{net} when the material is held at $T = T_{amb} = 300$ K. Consequently, $E_{b\lambda}(\lambda, T)$ is evaluated at 300 K and the parasitic heat flux is zero.

3. RESULTS AND DISCUSSIONS

3.1 Effect of Precursor Material Concentration

Initial attempts to electrospin PTFE alone proved unsuccessful, as nanobeads formed without the formation of nanofibers. These attempts provided valuable insight into the essential role of PEO as a necessary component in facilitating nanofiber formation.

To investigate the impact of precursor material concentration on the morphology and optical properties of electrospun coatings, we fabricated two samples, namely PP-1 and PP-2, containing precursor PTFE and PEO in ratios of 90:10 and 80:20, respectively. These coatings were electrospun using the following fabrication parameters: a volumetric flow rate of 8.33 µl/min, a potential of 10 kV between the needle and grounded collector, a collector-needle distance of 12 cm, and a rotating drum collector speed of 500 rpm. SEM images in Figures 2a and 2c depict the morphologies of these coatings, with corresponding fiber distributions shown in Figures 2b and 2d.

Observing the SEM images, we find that the composite structure consists of PTFE nanobeads (234 ± 59 nm) embedded within PEO nanofiber strands. Notably, under the same magnification (50k), composite fibers of PP-1 (Figures 2a and 2b) appear larger than those of PP-2 (Figures 2c and 2d). This observation is further supported by fiber distribution histograms, with PP-1 exhibiting an average fiber diameter of 1050 ± 174 nm, compared to 516 ± 87 nm for PP-2. PP-1 exhibits a higher concentration of PTFE nanobeads compared to PP-2, resulting in a greater number of beads adhering to the PEO nanofibers, thus contributing to the broader composite fibers.

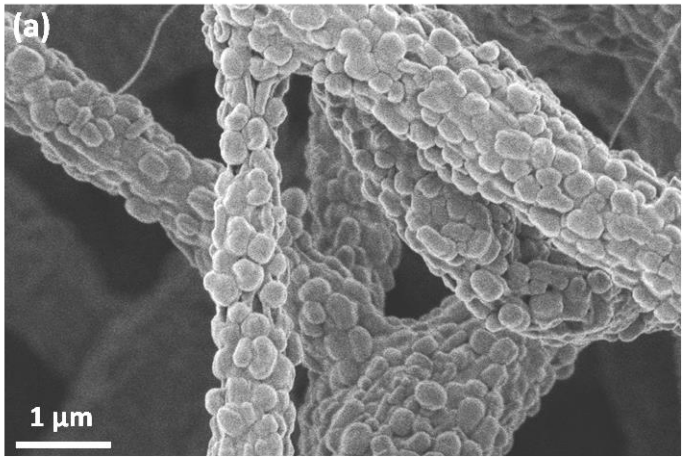

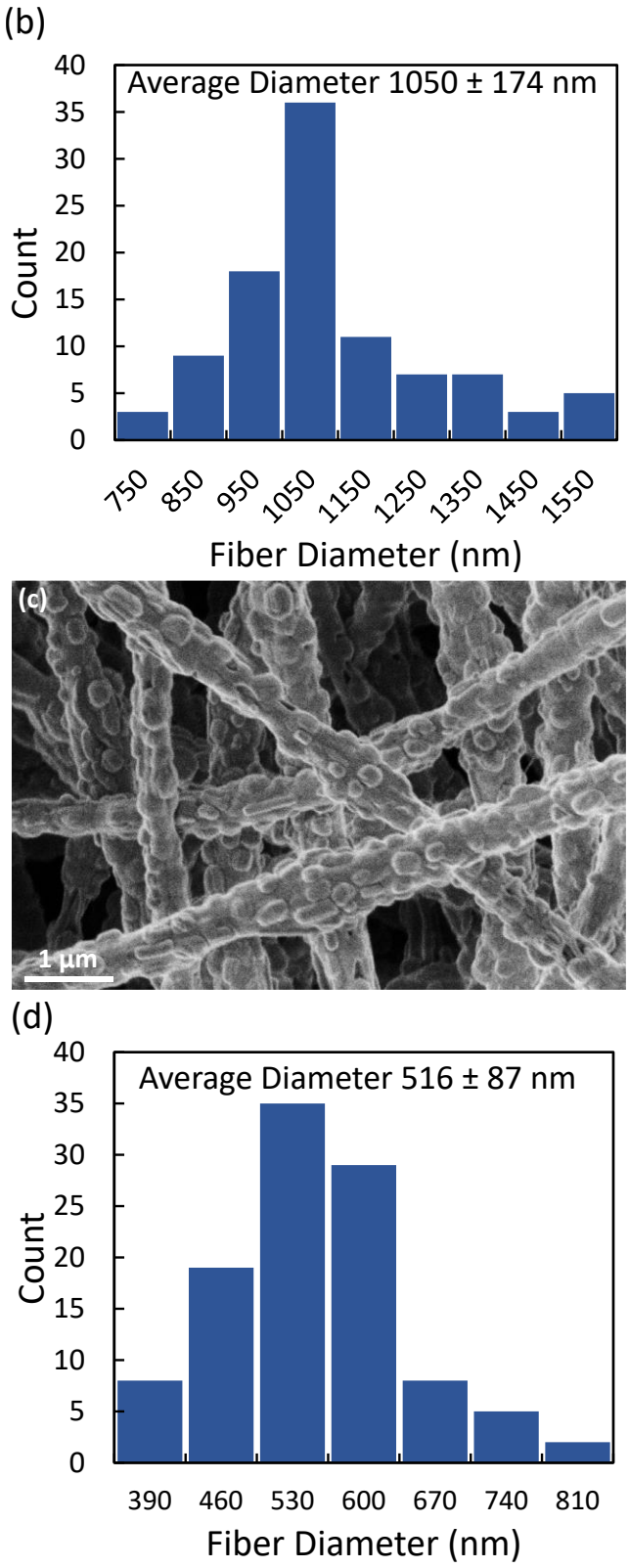

Figure 2: SEM images (50 k magnification) and fiber diameter distributions of samples PP-1 (a and b) and PP-2 (c and d) containing different ratios of the precursor materials.

Figure 3 presents the spectral normal-hemispherical reflectance of both samples across the 300-2500 nm spectral range, which encompasses the majority of solar spectral intensity. Additionally, the graph includes the overlay of terrestrial solar irradiance at AM 1.5.

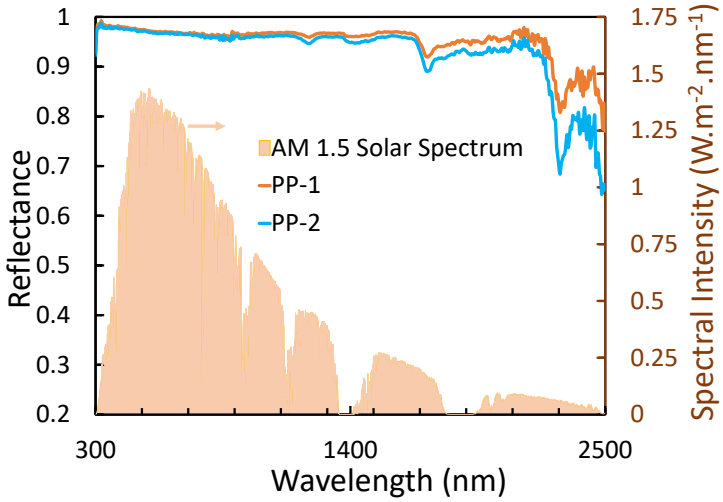

Figure 3: Spectral normal-hemispherical reflectance of samples PP-1 and PP-2 (left y-axis). AM 1.5 terrestrial solar spectral intensity (right y-axis) is shown for reference.

Both samples, each with a thickness of 0.3 mm, demonstrate exceptional reflectivity to incident solar radiation, as illustrated in Figure 3, with spectral reflectance nearing 100%. However, PP-1 exhibited a slightly higher average solar reflectance of 96.7% compared to PP-2 (96%). This marginal difference can be attributed to the larger fibers and broader distribution of fiber diameters in PP-1, which likely contributed to enhanced reflectance by scattering a wider range of incident radiation spectra compared to PP-2.

3.2 Effects of Rotating Collector Speed

The influence of the rotating collector's speed on coating morphologies was also investigated to elucidate its role in shaping the coatings. Two PP-1 samples with identical material concentrations were compared in this analysis. We maintained baseline fabrication parameters, including a volumetric flow rate of 8.33 µl/min, a potential of 10 kV between the needle and grounded collector, and a collector-needle distance of 12 cm. The rotating drum collector speed was varied, and we compared samples fabricated at 500 rpm and 2100 rpm. The findings are presented in Figure 4.

Figure 4a depicts the morphology of the sample fabricated at 500 rpm (PP-1 500 rpm), while its fiber diameter distribution is shown in Figure 4b. The SEM image (Figure 4a) illustrates a random orientation of composite nanofibers, with most fibers lacking a distinct alignment. In contrast, Figure 4c, representing the second sample fabricated at a significantly higher rotational

speed of 2100 rpm (PP-1 2100 rpm), displays a distinct orientation of fibers, with the majority aligned in a uniform direction.

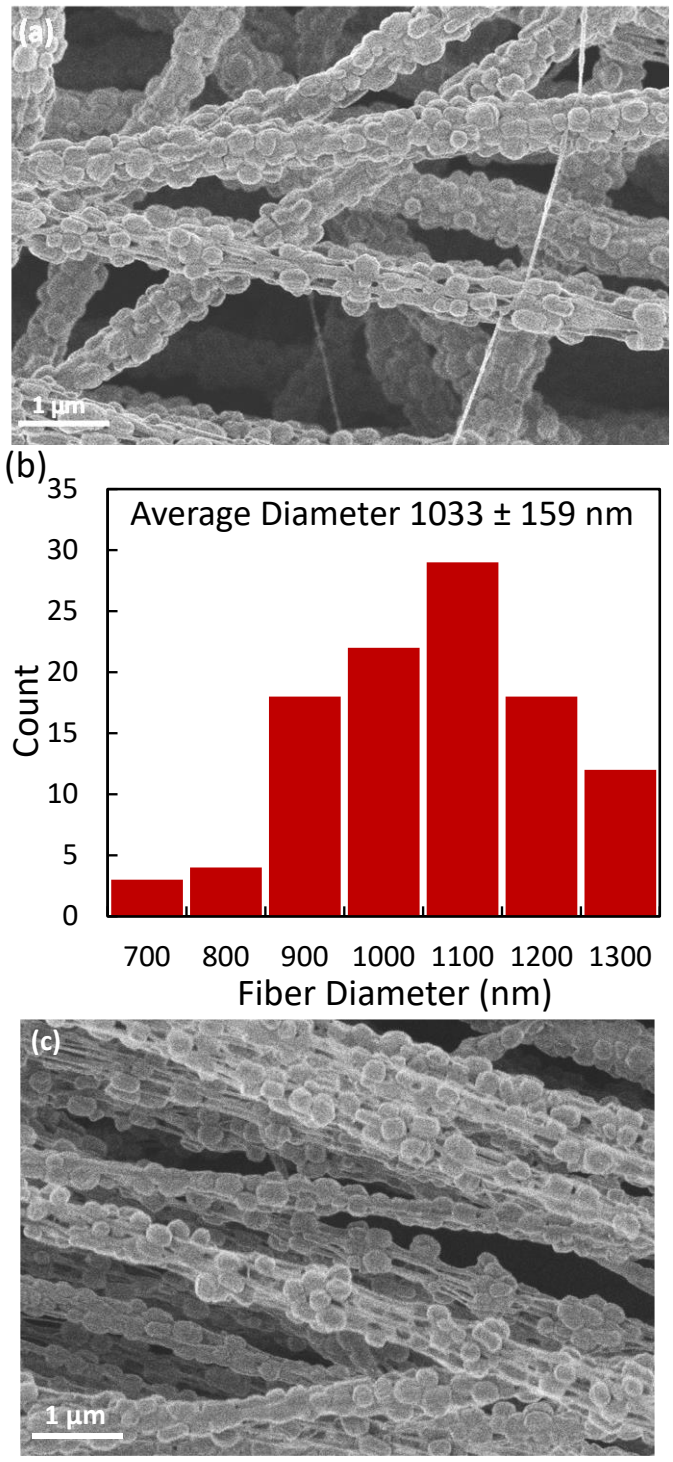

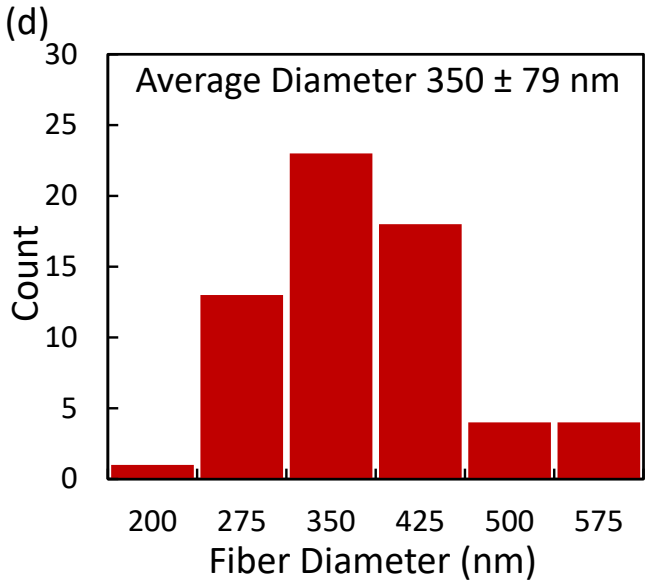

Figure 4: SEM images (50 k magnification) and fiber diameter distributions of samples PP-1 500 rpm (a&b) and PP-1 2100 rpm fabricated using different rotating drum collector speeds.

Figures 4b and 4d depict the fiber diameter distributions of PP-1 500 rpm and PP-1 2100 rpm, respectively. It is evident that PP-1 500 rpm, fabricated at a lower speed, exhibits significantly wider average fiber diameters (1033 ± 159 nm) compared to PP-1 2100 rpm (350 ± 79 nm), which is three times smaller. The increase in collector speed serves two main purposes: firstly, it promotes fiber alignment as the fibers have less time to randomly orient themselves on the collector; secondly, it leads to fiber stretching and thinning due to the higher torque exerted on the fibers during collection on the rotating collector.

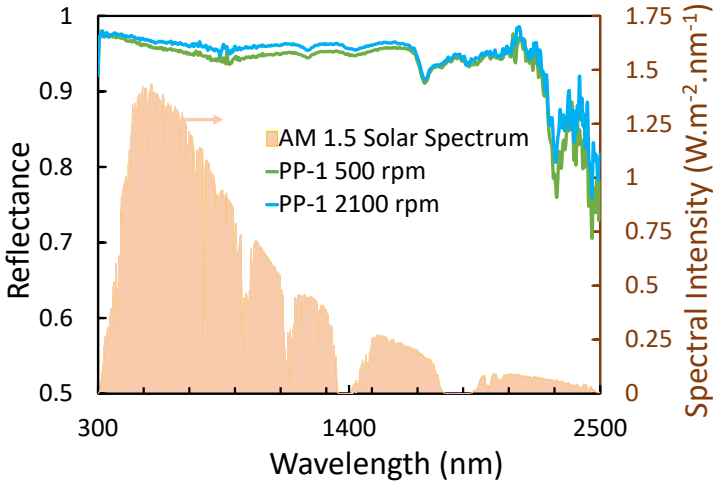

Figure 5: Spectral normal-hemispherical reflectance of samples PP-1 500 rpm and PP-1 2100 rpm (left y-axis). AM 1.5 terrestrial solar spectral intensity (right y-axis) is shown for reference.

Figure 5 presents the spectral normal-hemispherical reflectance of both samples across the 300-2500 nm spectral

range, with air mass 1.5 (AM 1.5) terrestrial solar irradiance overlaid on the graph. Both samples were of identical thickness (0.25 mm), and it is evident from the plot that PP-1 2100 rpm, with an average solar reflectance of 96.2%, slightly outperformed PP-1 500 rpm, which had an average solar reflectance of 95.2%.

The thinner and aligned fibers of PP-1 2100 rpm likely resulted in a denser fiber packing, reducing sample transmissivity marginally compared to PP-1 500 rpm. This difference, in turn, affects the propagation of incident radiation through the sample. A denser packing allows more fibers to diffusely scatter incoming light, leading to higher reflectance than a sample with less dense packing. Overall, both samples exhibited excellent optical performance, with reflectances approaching those of state-of-the-art materials.

3.3 Effects of Coating Thickness

In the preceding sections, we explored the impact of precursor materials and rotating drum speed on nanofiber morphology and solar reflectance, focusing on samples of uniform thickness. In this section, we investigate the influence of sample thickness on solar reflectance and thermal emittance. The fabrication of these samples maintained baseline parameters: a volumetric flow rate of 8.33 µl/min, 10 kV potential between the needle and grounded collector, a collector-needle distance of 12 cm, and a rotating drum collector speed of 500 rpm.

Figure 6a illustrates the spectral normal-hemispherical reflectance of three samples with thicknesses of 0.42 mm, 1.2 mm, and 3.36 mm (designated as PP-1 0.42 mm, PP-1 1.2 mm, and PP-1 3.36 mm, respectively) across the 300 – 2500 nm spectral range.

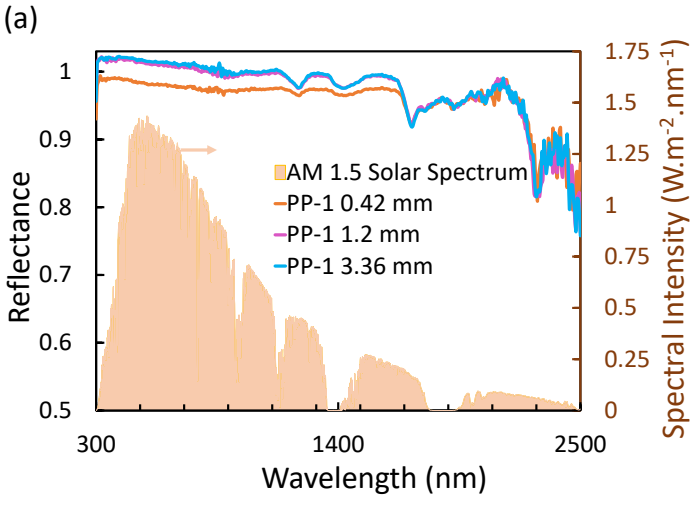

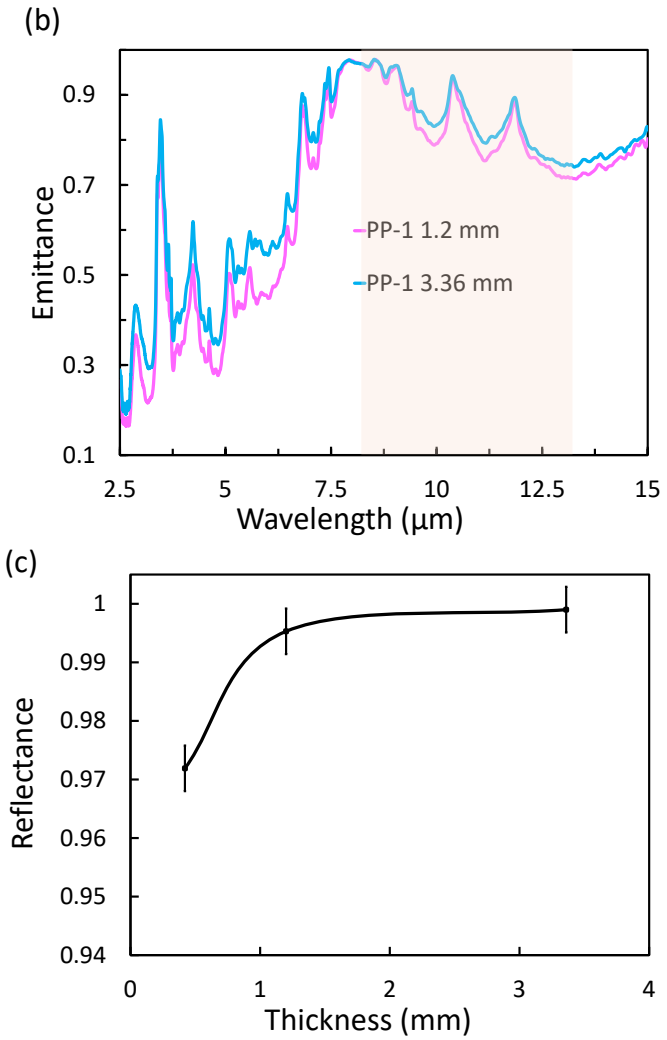

Figure 6: (a) Spectral normal-hemispherical reflectance of samples PP-1 0.42 mm, PP-1 1.2 mm and PP-1 3.36 mm, (left y-axis). (b) IR emittance of PP-1 1.2 mm and PP-1 3.36 mm. (c) Comparison of average solar reflectance with sample thickness.

It is evident from Figure 6a that reflectance increases notably with thickness. PP-1 0.42 mm exhibited an average solar reflectance of 97.2 ± 0.39 %, while PP-1 1.2 mm averaged 99.5 ± 0.39 %, and PP-1 3.36 mm reached 99.9 ± 0.4 %. This comparison underscores the significant impact of thickness on sample reflectance. Notably, the 99.9% reflectance achieved by PP-1 3.36 mm represents the highest reported reflectance for passive radiative cooling materials.

Figure 6b illustrates the spectral emittance (at 300 K) of PP-1 samples with thicknesses of 1.2 mm and 3.36 mm across the mid-infrared (MIR) and long-wave infrared (LWIR) spectral range (2.5 - 15 µm). Of particular significance is the emittance within the 8 - 13 µm range, which corresponds to the atmospheric transmission window. Within this wavelength range, materials can effectively couple with outer space at a temperature of 3 K, emitting thermal radiation and facilitating

cooling. PP-1 1.2 mm exhibited an average emittance of 84.42% within the atmospheric transmission window, while PP-1 3.36 mm averaged 86.69% within the same range (8-13 μm), indicating strong thermal emission capabilities for both samples, enabling self-cooling.

Figure 6c compares the average solar reflectance of samples with varying thicknesses. It is evident from the graph that reflectance surpasses 99% beyond a thickness of 1 mm and saturates at 99.9% for thicknesses exceeding 3 mm.

4. RADIATIVE COOLING PERFORMANCE

Radiative cooling analysis was conducted on PP-1 samples with thicknesses of 1.2 mm and 3.36 mm, considering their optical properties. The analysis yielded the following cooling power densities (Table 1). Both materials exhibited exceptional performance, with PP-1 3.36 mm achieving a net cooling power exceeding 106 W/m^2. Such a substantial cooling capacity would lead to a sizeable reduction in the need for active cooling in buildings and cars.

Table 1. Radiative Cooling Performance of PP-1 Samples

Material	P_{out} (W/m^2)	P_{atm} (W/m^2)	P_{solar} (W/m^2)	P_{net} (W/m^2)
PP-1 1.2 mm	202.99	98.6	4.46	**99.93**
PP-1 3.36 mm	211.03	103.65	0.89	**106.49**

5. COMPARISON WITH STATE-OF-THE-ART PASSIVE RADIATIVE COOLING MATERIALS

Since passive radiative cooling performance is lowered when the materials have high solar absorptance (α_s), it is necessary to develop materials with large solar reflectance ($\alpha_s = 1 - \rho_s$). Likewise, a strong LWIR emittance is desirable in the atmospheric transmission window (ε_{ATW}) to enable self-cooling. Considering both aspects, the figure of merit, $\varepsilon_{ATW}/\alpha_s$ should be large for high-performance radiative cooling materials.

Figure 7 compares the figure of merit, $\varepsilon_{ATW}/\alpha_s$ for various state-of-the-art passive radiative cooling materials having low α_s and high ε_{ATW}. Specifically, since this study considers a surface held at 300 K, we compare $\varepsilon_{ATW,300K}/\alpha_s$ for different passive thermal control materials with the electrospun materials developed in this study. Figure 7 shows that the electrospun materials outperform the state-of-the-art by orders of magnitude, indicating that they would perform remarkably well as passive radiative cooling materials.

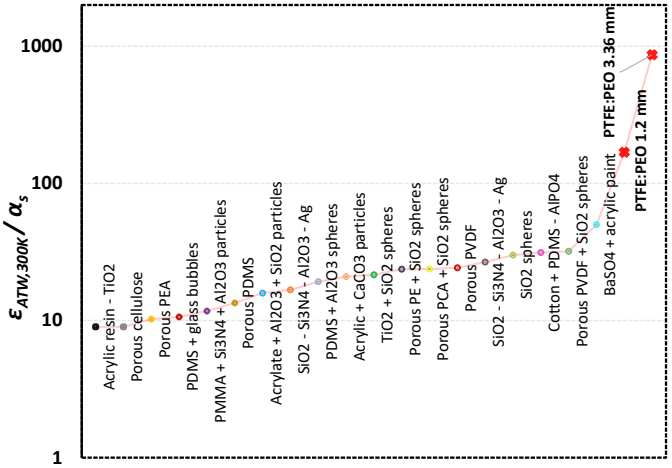

Figure 7: Comparison between the electrospun PTFE:PEO coatings with state-of-the-art terrestrial passive radiative cooling materials.

6. CONCLUSION

In this study, we have successfully developed passive thermal control coating materials tailored for terrestrial applications. Utilizing the electrospinning fabrication technique, we engineered coating materials with a nano- and micro-scale porous structure, ideal for efficient scattering of incident light. This investigation elucidates the influence of manufacturing parameters such as rotating collector speed, precursor material concentration, and sample thickness on both morphology and optical performance.

Notably, the electrospun materials developed in this study exhibit exceptionally high solar reflectance, indicating minimal solar absorption and high thermal emittance within the electromagnetic spectrum's mid and long-wave infrared regions. Of significant importance, we achieved an average solar reflectance of 99.9% (relative to Spectralon's®), marking one of the highest reported values in the literature.

Through radiative cooling performance analysis, we obtained net cooling powers of 99.9 and 106.5 W/m^2 for the materials developed in this study, underscoring their passive radiative capability. Moreover, a comparison of the figure of merit, $\varepsilon_{ATW}/\alpha_s$, with other state-of-the-art passive radiative cooling materials reveals orders of magnitude higher performance. Consequently, our findings suggest that the developed materials hold significant promise as highly efficient passive cooling solutions for various applications.

ACKNOWLEDGEMENTS

The authors acknowledge the support of the National Aeronautics and Space Administration under Grant No.

80NSSC21K0072 issued through the Space Technology Research Grants.

REFERENCES

[1] Selvadurai S, Chandran A, Valentini D, Lamprecht B. Passive Thermal Control Design Methods, Analysis, Comparison, and Evaluation for Micro and Nanosatellites Carrying Infrared Imager. Applied Sciences (Switzerland) 2022;12. https://doi.org/10.3390/app12062858.

[2] Consulting Inc N. Energy Savings Potential and RD&D Opportunities for Commercial Building HVAC Systems. 2017.

[3] Zhou K, Li W, Patel BB, Tao R, Chang Y, Fan S, et al. Three-Dimensional Printable Nanoporous Polymer Matrix Composites for Daytime Radiative Cooling. Nano Lett 2021;21:1493–9. https://doi.org/10.1021/acs.nanolett.0c04810.

[4] Chen M, Pang D, Mandal J, Chen X, Yan H, He Y, et al. Designing Mesoporous Photonic Structures for High-Performance Passive Daytime Radiative Cooling. Nano Lett 2021;21:1412–8. https://doi.org/10.1021/acs.nanolett.0c04241.

[5] Wang X, Narayan S. Thermal radiative switching interface for energy-efficient temperature control. Renew Energy 2022;197:574–82. https://doi.org/10.1016/j.renene.2022.07.143.

[6] Zhang J, Zhou Z, Tang H, Xing J, Quan J, Liu J, et al. Mechanically Robust and Spectrally Selective Convection Shield for Daytime Subambient Radiative Cooling 2021. https://doi.org/10.1021/acsami.0c21204.

[7] Nie X, Yoo Y, Hewak H, Sullivan J, Krishna A, Lee J. Cool White Polymer Coatings based on Glass Bubbles for Buildings 2020:1–10. https://doi.org/10.1038/s41598-020-63027-2.

[8] Han D, Fei J, Mandal J, Liu Z, Li H, Raman AP. Solar Energy Materials and Solar Cells Sub-ambient radiative cooling under tropical climate using highly reflective polymeric coating. Solar Energy Materials and Solar Cells 2022;240:111723. https://doi.org/10.1016/j.solmat.2022.111723.

[9] Zhai Y, David SN, Zhao D, Lou R, Tan G, Yang R. Scalable-manufactured randomized glass-polymer hybrid metamaterial for daytime radiative cooling 2017;1066:1062–6.

[10] Li D, Liu X, Li W, Lin Z, Zhu B, Li Z, et al. Scalable and hierarchically designed polymer film as a selective thermal emitter for high-performance all-day radiative cooling 2021;16. https://doi.org/10.1038/s41565-020-00800-4.

[11] Raman AP, Anoma MA, Zhu L, Rephaeli E, Fan S. Passive radiative cooling below ambient air temperature under direct sunlight 2014. https://doi.org/10.1038/nature13883.

[12] Li M, Wang X, Odom L, Bryce K, Zhao D, Shen J, et al. Three-Dimensional Hollow Reduced Graphene Oxide Tube Assembly for Highly Thermally Conductive Phase Change Composites and Efficient Solar-Thermal Energy Conversion. ACS Appl Mater Interfaces 2023;15:18940–50. https://doi.org/10.1021/acsami.3c00546.

[13] Wang X, Hsieh ML, Bur JA, Lin SY, Narayanan S. The role of nanostructure morphology of nickel-infused alumina on solar-thermal energy conversion. Journal of Optics (United Kingdom) 2021;23. https://doi.org/10.1088/2040-8986/abcc53.

[14] Wang X, Hsieh ML, Bur JA, Lin SY, Narayanan S. Capillary-driven solar-thermal water desalination using a porous selective absorber. Mater Today Energy 2020;17. https://doi.org/10.1016/j.mtener.2020.100453.

[15] Wang X, Repolho Cagliari LV, Hicken JE, Narayan S. Optimization of nickel-infused alumina nanostructure for enhanced solar-thermal conversion. MRS Commun 2023;13:581–6. https://doi.org/10.1557/s43579-023-00386-7.

[16] Ibekwe C, Wang X, Bolzani BN, O'Brien C, Waataja CJ, Mahony CP, et al. Synthesis, Optical Performance Characterization, and Durability of Electrospun PTFE-PEO Materials for Space Applications. ACS Appl Mater Interfaces 2024. https://doi.org/10.1021/acsami.4c02463.

[17] Yang P, Chen C, Zhang ZM. A dual-layer structure with record-high solar reflectance for daytime radiative cooling. Solar Energy 2018;169:316–24. https://doi.org/10.1016/j.solener.2018.04.031.

[18] Gamage S, Banerjee D, Alam MM, Hallberg T, Åkerlind C, Sultana A, et al. Reflective and transparent cellulose-based passive radiative coolers. Cellulose 2021;28:9383–93. https://doi.org/10.1007/s10570-021-04112-1.

[19] Suichi T, Ishikawa A, Tanaka T, Hayashi Y, Tsuruta K. Whitish daytime radiative cooling using diffuse reflection of non-resonant silica nanoshells. Sci Rep 2020;10:1–6. https://doi.org/10.1038/s41598-020-63591-7.

[20] Li X, Peoples J, Huang Z, Zhao Z, qiu jun, Ruan X. Full Daytime Sub-Ambient Radiative Cooling with High Figure of Merit in Commercial-Like Paints. SSRN Electronic Journal 2020. https://doi.org/10.2139/ssrn.3652325.

[21] Chae D, Kim M, Jung PH, Son S, Seo J, Liu Y, et al. Spectrally Selective Inorganic-Based Multilayer Emitter for Daytime Radiative Cooling. ACS Appl Mater Interfaces 2020;12:8073–81. https://doi.org/10.1021/acsami.9b16742.

[22] Zhang X, Yang L, Wang F, Cheng Z, Liang H. Wrinkled surface microstructure for enhancing the infrared spectral performance of radiative cooling. Opt Express 2021;29:11416. https://doi.org/10.1364/oe.418650.

[23] Xiang B, Zhang R, Luo Y, Zhang S, Xu L, Min H, et al. 3D porous polymer film with designed pore architecture and auto-deposited SiO2 for highly efficient passive radiative cooling. Nano Energy 2021;81:105600. https://doi.org/10.1016/j.nanoen.2020.105600.
[24] Zhou L, Song H, Liang J, Singer M, Zhou M, Stegenburgs E, et al. A polydimethylsiloxane-coated metal structure for all-day radiative cooling Lyu 2019;2.
[25] Bhardwaj N, Kundu SC. Electrospinning: A fascinating fiber fabrication technique. Biotechnol Adv 2010;28:325–47. https://doi.org/10.1016/j.biotechadv.2010.01.004.
[26] Doshi J, Reneker DH. Electrospinning process and applications of electrospun fibers. Conference Record - IAS Annual Meeting (IEEE Industry Applications Society) 1993;3:1698–703. https://doi.org/10.1109/ias.1993.299067.
[27] Ding B, Li C, Miyauchi Y, Kuwaki O, Shiratori S. Formation of novel 2D polymer nanowebs via electrospinning. Nanotechnology 2006;17:3685–91. https://doi.org/10.1088/0957-4484/17/15/011.
[28] Gibson P, Schreuder-Gibson H, Pentheny C. Electrospinning Technology: Direct Application of Tailorable Ultrathin Membranes. Journal of Industrial Textiles 1998;28:63–72. https://doi.org/10.1177/152808379802800106.
[29] Huang Y, Huang QL, Liu H, Zhang CX, You YW, Li NN, et al. Preparation, characterization, and applications of electrospun ultrafine fibrous PTFE porous membranes. J Memb Sci 2017;523:317–26. https://doi.org/10.1016/j.memsci.2016.10.019.
[30] Xiong J, Huo P, Ko FK. Fabrication of ultrafine fibrous polytetrafluoroethylene porous membranes by electrospinning. J Mater Res 2009;24:2755–61. https://doi.org/10.1557/jmr.2009.0347.
[31] Zhang F, Si Y, Yu J, Ding B. Electrospun porous engineered nanofiber materials: A versatile medium for energy and environmental applications. Chemical Engineering Journal 2023;456:140989. https://doi.org/10.1016/j.cej.2022.140989.
[32] Park YS, Kim J, Oh JM, Park S, Cho S, Ko H, et al. Near-Field Electrospinning for Three-Dimensional Stacked Nanoarchitectures with High Aspect Ratios. Nano Lett 2020;20:441–8. https://doi.org/10.1021/acs.nanolett.9b04162.
[33] Li D, Wang Y, Xia Y. Electrospinning Nanofibers as Uniaxially Aligned Arrays and Layer-by-Layer Stacked Films. Advanced Materials 2004;16:361–6. https://doi.org/10.1002/ADMA.200306226.
[34] Nowak JF, Clippinger A, Samuel J. Freeform fabrication of fiber-reinforced hydrogels using direct-write far-field electrospinning. J Manuf Process 2020;58:955–63. https://doi.org/10.1016/j.jmapro.2020.08.041.

